

This work was written as part of one of the author's official duties as an Employee of the United States Government and is therefore a work of the United States Government. In accordance with 17 U.S.C. 105, no copyright protection is available for such works under U.S. Law.

Public Domain Mark 1.0

<https://creativecommons.org/publicdomain/mark/1.0/>

Access to this work was provided by the University of Maryland, Baltimore County (UMBC) ScholarWorks@UMBC digital repository on the Maryland Shared Open Access (MD-SOAR) platform.

Please provide feedback

Please support the ScholarWorks@UMBC repository by emailing scholarworks-group@umbc.edu and telling us what having access to this work means to you and why it's important to you. Thank you.

JGR Atmospheres

RESEARCH ARTICLE

10.1029/2022JD036636

Special Section:

Monitoring the Earth radiation budget and its implication to climate simulations: Recent Advances and Discussions

Key Points:

- The probability density function of the top of atmosphere shortwave (TOA SW) flux is not normally distributed but positively skewed, with a near-global median value of ~ 3 W/m² less than the mean
- Hemispheric asymmetry exists with the 10:30 a.m. local time TOA SW observations from Terra platform. SH reflects about 1–4 W/m² more SW flux than NH, with the MISR and CERES Single Scanner Footprint (SSF1deg) products observed from Terra
- While the characteristics of the MISR and CERES SW fluxes broadly agree with each other, differences in the regional PDF from the two SW fluxes are substantial over the high cloud and high altitude regions

Correspondence to:

J. N. Lee,
jae.n.lee@nasa.gov

Citation:

Lee, J. N., & Wu, D. L. (2022). Non-Gaussian distributions of TOA SW flux as observed by MISR and CERES. *Journal of Geophysical Research: Atmospheres*, 127, e2022JD036636. <https://doi.org/10.1029/2022JD036636>



Received 14 FEB 2022

Accepted 16 JUN 2022

© 2022. The Authors.

This is an open access article under the terms of the [Creative Commons Attribution License](#), which permits use, distribution and reproduction in any medium, provided the original work is properly cited.

Non-Gaussian Distributions of TOA SW Flux as Observed by MISR and CERES

Jae N. Lee^{1,2}  and Dong L. Wu² 

¹Joint Center for Earth Systems Technology, University of Maryland, Baltimore County, Baltimore, MD, USA, ²NASA Goddard Space Flight Center, Greenbelt, MD, USA

Abstract The Top of Atmosphere (TOA) shortwave (SW) flux, converted from Terra Multi-angle Imaging SpectroRadiometer (MISR) narrow band albedos, is compared with that measured from Clouds and the Earth's Radiant Energy System (CERES). We describe the probability density function (PDF) of the monthly TOA SW flux and how the statistical third moment, skewness, can impact the quantification of the flux. The PDF of the SW flux is not normally distributed but positively skewed. In both sets of observations, the near-global (80 S–80 N) median value of the SW flux is ~ 3 W/m² less than the mean value, due to the positive skewness of the distribution. The near-global mean TOA SW flux converted from MISR is about 7 W/m² ($\sim 7\%$) less than CERES measured flux during the last two decades. Surprisingly, a hemispheric asymmetry exists with TOA SW observations from the Terra platform. SH reflects 3.92 and 1.15 W/m² more mean SW flux than NH, from MISR and CERES Single Scanner Footprint products, respectively. We can infer that the offsetting by morning clouds in the SH is greater than the effect of hemispheric imbalance of SW flux caused by different land masses in two hemispheres. While the characteristics of the two SW fluxes broadly agree with each other, differences in the regional PDF from two different SW fluxes are substantial over high cloud regions and high altitude regions. Our analysis shows that some parts of the different skewness from the two measurements may be attributed to the different calibration of the radiance anisotropy over high cloud scenes.

Plain Language Summary In this work, we describe the non-Gaussian probability density functions (PDFs) of the Top of Atmosphere (TOA) reflected shortwave (SW) flux. For non-Gaussian PDFs, the frequency of occurrence is not symmetric with respect to the mean. The TOA SW PDFs are relatively thick in the left tail because there exists a low boundary of zero reflectance when the Earth don't get solar insolation during the polar nights. In a comparison of two satellite measurements, we show how the statistical third moments of the TOA SW flux can impact the quantification of the averaged flux. Gaussian distributions are naturally assumed in atmospheric data analysis. This, however, is not always true for the TOA SW flux distribution. The two instruments, Multi-angle Imaging SpectroRadiometer (MISR) and Clouds and the Earth's Radiant Energy System (CERES), on the Earth Observing System Terra satellite (launched in December of 1999) offer a rare opportunity to observe the TOA reflected SW flux from the same constellation. Hemispheric asymmetry exists at 10:30 a.m. local time TOA SW observations from Terra platform. SH reflects about 1–4 W/m² more SW flux than NH, with the MISR and CERES Single Scanner Footprint (SSF1deg) products observed from Terra.

1. Introduction

Quantifying the amount of solar insolation reflected back to space at the top of the atmosphere (TOA) is pivotal for an assessment of Earth's radiation balance (Loeb & Wielicki, 2015; L'Ecuyer, 2017; Stephens et al., 2012; Trenberth, 2009; Wild et al., 2015). This reflected SW energy is initially forced by diurnal and seasonal variations of the incoming solar insolation. Caused by the obliquity of the Earth, each hemisphere receives more solar radiation during its summer when the hemisphere is tilted toward the Sun and less during winter when it is tilted away. The distribution of TOA reflected SW flux (TOA SW flux) is a mixture of complex multiple processes of the surface and atmospheric reflection from different types of surface and atmospheric conditions. Furthermore, the hemispheric asymmetry of the global land and ocean masses builds on additional complexity in the characterization of the TOA SW flux. The 11-year solar cycle variation of the solar insolation also can be factored into the decadal variations, however, the direct effect of solar cycle forcing is expected to be negligible as its magnitude is less than 0.01% (Kopp & Lean, 2011).

In addition to the accurate assessment of mean (μ) and standard deviation (σ) of the flux, it is imperative to characterize the normality of TOA SW flux distribution because the TOA SW flux distribution reflects the hemispheric asymmetry of solar insolation and land masses. A Gaussian or normal distribution is a type of probability distribution for a random variable, as the probability density function (PDF) is symmetric on either side of the mean with no skewness. Partly due to the central limit theorem (Feller, 1971) which states the average of many observations of a random variable approaches a normal distribution, the mean of the normal distributions is commonly used to represent observed and modeled large-scale atmospheric and oceanic variables. However, in fact, the normality of the distribution is one of the underlying assumptions in data analysis. When PDFs have deviated from the normal distribution, they are not well characterized by the μ and σ . Not like a normal distribution, it would be insufficient to deduce the states of tail probabilities even if the changes of μ and σ are accurately estimated. The skewness of the distribution can cause complexity in quantifying trends (Sardeshmukh et al., 2015) because the shape of the heavy tail, high reflected flux in the TOA SW case, may not be preserved with fastly vanishing high-latitude snow and ice. In a warmer climate, a regional mean may change with the same skewness, but it is also possible that the mean does not change with different distribution of the flux.

In this work, we describe the non-Gaussian PDFs of TOA SW flux, in comparison to two satellite measurements from MISR and CERES, and how the statistical third moments of the TOA SW flux can impact the quantification of the globally averaged flux. We also quantify the hemispheric differences of TOA SW flux between NH and SH and how they are dependent on observing the constellation of Terra and Aqua.

To quantify the global climatology of TOA SW flux, reliable and consistent satellite measurement is required. The two instruments, MISR and CERES, on the Earth Observing System Terra satellite (launched in December of 1999) offer a rare opportunity to observe the TOA reflected SW flux from the same constellation. Since no space-based measurement, so far, can measure radiances in all viewing angles simultaneously, the radiance-to-flux conversion has been recognized as a major source of uncertainty in the satellite-derived TOA SW flux (Loeb et al., 2006). Even after considerable improvements in Angular Distribution Models (ADMs), challenges are still remaining in the radiance to flux conversion, due to ADMs' strong dependence on clouds and high-albedo surfaces (Gristey et al. [2021]; Loeb et al. [2007, 2018] and references therein).

The MISR instrument provides information on bidirectional reflectance anisotropy (Diner et al., 2005) and inconsistency between the MISR and CERES fluxes can be largely attributed to limitations in the integration of bidirectional reflectance and ADMs (Loeb et al., 2006). Over the overcast ocean scenes within 75S–75 N, the uncertainty in the MISR albedos due to narrow-to-broadband albedo conversion is $\sim 2\%$. The difference between the MISR and CERES albedos due to the angular distribution model (ADM) is estimated to be $\sim 4\%$ (Sun et al., 2006).

2. Data

2.1. MISR

MISR's arrangement of nine cameras provides near-simultaneous measurements of reflective SW radiances from multi-angle views in four spectral bands (Diner et al., 1998). Reflected SW spectral radiances are measured at nadir and at 26.1°, 45.6°, 60°, and 70.5° forward and aft of nadir along the satellite track, in blue (446 ± 21 nm), green (558 ± 15 nm), red (672 ± 11 nm), and near-infrared (866 ± 20 nm) bands. By deriving albedos from nine angular measurements, MISR has the advantage of retrieving accurate albedos for inhomogeneous clouds (Diner et al. [2005]; MISR ATBD, <https://eosps0.gsfc.nasa.gov/sites/default/files/atbd/atbd-misr-08.pdf>).

MISR produces three TOA spectral albedo products; local, restrictive, and expansive albedos. Local albedo estimates the reflected flux passing through an unobscured 2.2 km domain reflecting the level of reference altitude. The restrictive albedo is an estimate of the reflected flux which originates from the reflecting surfaces within the 35 km domain. The expansive albedo is an estimate of the flux passing through the TOA regardless of where it is reflected.

We used the restrictive albedos in this study since it is a useful measure of scene-dependent properties and most analogous to the CERES determination of the TOA albedo from a single view.

The methodology applied to compute MISR broadband albedo involves a regression of 4 spectral narrow band albedos onto CERES broadband albedo (Sun et al., 2006). Then broadband MISR restrictive albedo (α) is converted to TOA SW flux by multiplying incident solar insolation (S_0) at a given time and location, that is,

TOA SW flux = $\alpha \cdot S_0$. Incident solar insolation, S_0 , is acquired from the CERES SSF1deg product at a given time and location.

In this study, we utilized the restrictive broadband albedos from MISR Level-3 albedo product (Diner, 2009), from March 2000 to December 2020, from NASA Atmospheric Science Data Center (<https://asdc.larc.nasa.gov/documents/misr/version/pge12b.html>). Given the sampling nature of the MISR observation, we used monthly mean data products.

2.2. CERES

The CERES Edition 4.1 monthly mean 1° gridded Single Scanner Footprint (SSF1deg) TOA SW flux products from Terra and Aqua satellite (Doelling, 2015) and Energy Balanced and Filled (EBAF) products (Doelling, 2019) are analyzed to be compared with converted broadband MISR flux. The SSF1deg product began in March 2000 and provides global coverage sampled only at specific times of the day (Doelling et al., 2013). As well as MISR, the CERES instrument on EOS Terra measures TOA SW flux in a sun-synchronous ascending orbit with an equator crossing time of near 10:30 a.m. local time. The CERES albedo retrieval is based on a set of combined empirical and theoretical scene-dependent ADMs (Ham et al., 2015; Kato, 2005; Loeb et al., 2005, 2009; Su et al., 2015a, 2015b; and references there in). The selection of ADMs depends on the cloud types and a cloud parameter which is determined by the cloud fraction, optical depth, cloud height, and phase of clouds.

In this study, we focused on examining the consistencies and differences of the TOA SW flux from the MISR and CER_SSF_Terra-FM1-MODIS_Edition4A datasets. Where MISR data is not available in high latitudes, we also omitted CERES data for a fair comparison. We obtained the CERES SSF1deg monthly TOA SW and cloud height data from (<https://ceres-tool.larc.nasa.gov/ord-tool/jsp/SSF1degEd41Selection.jsp>).

3. Results

3.1. Non-Normality of the TOA SW Flux

In this section, we describe the non-Gaussian distributions of TOA SW flux, in comparison to two satellite measurements from MISR and CERES. As shown in Figure 1, the PDFs of MISR and CERES TOA SW flux are not only non-Gaussian but are distinctly skewed distributions which have more population of the data on the right side of the maximum population. The PDFs of the monthly broadband TOA SW flux from MISR and CERES are shown in Figure 1a, where the area under the PDF accounts for the near-global (80S - 80N) distribution of monthly mean TOA SW flux at each 1° by 1° grid. The distribution of the data indicates that the monthly mean TOA SW flux extends from 0 to 410 W/m².

The PDFs of broadband flux show one major peak at 58 and 65 W/m² for MISR and CERES, respectively. While the general features of PDFs of the near-global TOA SW distribution from the two observations are in good agreement with ~7 W/m² offset at the peak, they commonly show that SW fluxes are obviously not normally distributed. The right side of the distribution is heavily tailed with high reflectance values from snow and ice, but the left side of the distribution has no tails. The PDFs are relatively thick in the left tail because TOA SW flux cannot be negative with a low boundary of zero reflectance when they don't get solar insolation during the polar nights.

Similarly, the PDFs of the four narrow band MISR TOA SW fluxes centered at blue (C1: 446 ± 21 nm), green (C2: 558 ± 15 nm), red (C3: 672 ± 11 nm), and near-infrared (C4: 866 ± 20 nm) are shown in Figure 1b. The four spectral PDFs also show similar skewed non-Gaussian features.

For a Gaussian or Normal distribution, the PDF is symmetric on either side of the mean. Without any prior assumptions, the TOA SW distributions deviate from the normal distribution, they are not well characterized by the μ and σ . Not like a normal distribution, it would be insufficient to deduce the changes in tail probabilities from the μ and σ , even if the changes of μ and σ are accurately estimated.

Skewness is a measure of the asymmetry of the probability distribution about its mean. Conventionally, positive skewness indicates that more populations of data are located on the right trail from the maximum population. Reflecting the positive skewness, the TOA SW flux distributions show that more populations are present on the right side of the distribution where the fluxes are larger than the mean or median. The right tail of the SW flux

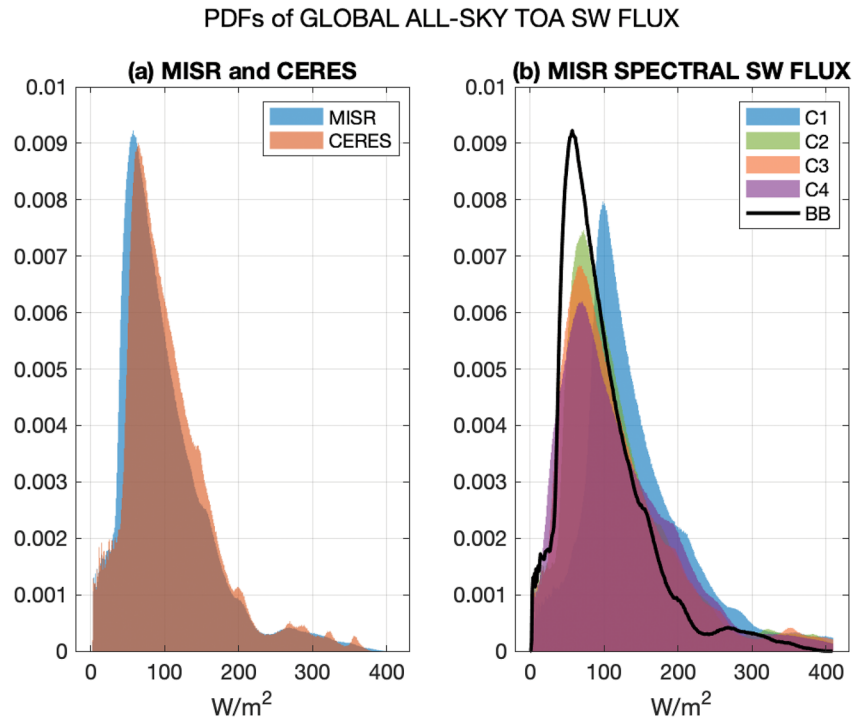


Figure 1. (a) Probability density functions (PDFs) of the monthly mean near-global (80S–80 N) distribution of all-sky broadband Top of Atmosphere (TOA) shortwave (SW) Flux (W/m^2) measured from multiangle imaging spectroradiometer (MISR) and Clouds and the Earth's Radiant Energy System. We analyze 240 monthly samples at each grid points for 2001–2020. MISR broadband (BB) TOA SW flux (W/m^2) is converted from four narrow band albedos. The bin size is 1 W/m^2 , and the total integration of the area under each PDF is normalized to be one. (b) Four narrow bands, Channel 1 - Channel 4 (C1 - C4) MISR TOA SW flux (W/m^2) centered at blue, green, red, and near-infrared. MISR broadband flux is overlaid with a black curve.

distribution is extremely important since the high flux greater than 300 W/m^2 is from the Arctic and Antarctic regions over high albedo snow and ice surface. The right tail of the SW flux is also related to cloud properties and estimating the average flux without considering cloud types may cause systematic biases (Barkett et al., 1996). The skewness of the distribution can add complexity to quantifying global TOA SW climatologies and trends because the shape of the distribution may not be preserved with a changing environment. For example, fastly vanishing high-latitude snow and ice can cause a thickening of the right tail without affecting the left tail of the distribution.

Figure 2 is a schematic of the MISR TOA SW flux, which shows the PDF deviated from the normal distribution. The mean and the standard deviation of the not area-weighted near-global monthly mean SW flux from MISR (80S - 80N) are 98.6 W/m^2 , and 66.19 W/m^2 , respectively. The global (90S–90 N), annual mean all-sky TOA SW flux from CERES Energy Balanced and Filled (EBAF) data was 99.7 W/m^2 , which is equivalent to a global albedo of 0.293 (Stephens et al., 2015).

The red curve of the plot is the best-fit normal distribution with the same mean and standard deviation from MISR. The yellow curve is a normal distribution with a mean at the mode, where the most population is located. The blue curve is a best-fit lognormal distribution using the log of TOA SW flux values. The median of the distribution is 83.68 W/m^2 , which is $\sim 15 \text{ W/m}^2$ less than the mean. While the TOA SW flux distribution deviated from the normal distribution, it is rather close to the lognormal distribution with mean (m) and standard deviation (v) of 4.46 and 0.63 W/m^2 , respectively. The lognormal distribution can be potentially utilized to estimate the true mean and variance of the TOA SW flux in future work, however, the conversion of the lognormal to the normal distribution is very sensitive to the parameters of the lognormal distribution, that is, m and v , since the true mean (μ) and standard deviation (σ) of the original distribution can be acquired from the exponential function of m and v . We also analyzed the PDFs of the daily TOA SW flux and they show similar non-Gaussian features. In fact, the

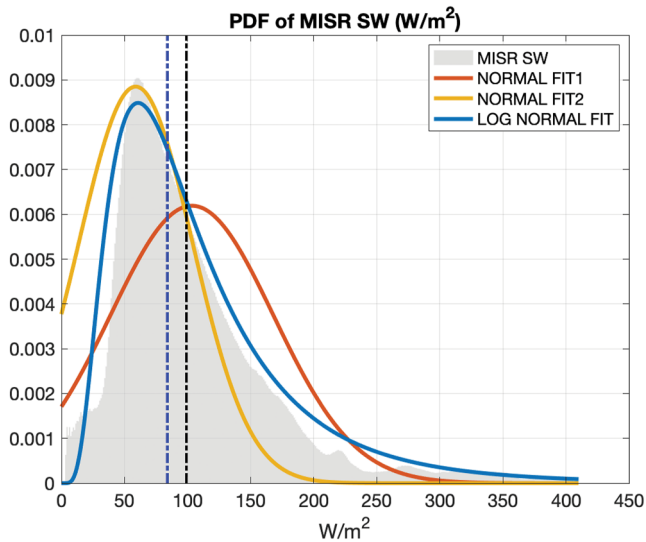


Figure 2. Deviation of probability density functions (PDFs) of multiangle imaging spectroradiometer (MISR) Top of Atmosphere (TOA) shortwave (SW) flux (W/m^2) from normal distribution. The PDF is for MISR TOA SW Flux, as described in Figure 1a. The blue curve is a best-fit lognormal distribution of the TOA SW flux values. The red curve is a best-fit normal distribution using the mean and the standard deviation of the TOA SW flux. The yellow curve is a hypothetical normal distribution with a mean at the mode of the flux distribution. The black and blue dotted line represents the mean and median value of the SW flux, respectively.

PDFs of the daily flux can be more useful for a lognormal fit since they are smoother with more samples, compared to the monthly PDFs.

We generated climatologies (2001–2020) for MISR and CERES TOA SW flux on a $1^\circ \times 1^\circ$ spatial scale, by taking not only the monthly mean averages but also taking median values of SW flux at each grid over a period under study. To find the region where the temporal distribution deviated from the normal distribution, we estimated the difference in climatology of the mean and the median by subtracting the mean climatology from the median climatology, that is, $\text{MEDIAN} - \text{MEAN}$ at each grid point. Figures 3a and 3b show the spatial distributions of the difference between the median climatology and the mean climatology within $60^\circ\text{S} - 60^\circ\text{N}$ from MISR and CERES, respectively. The similarities of each figure from two different measurements indicate that the difference between median and mean is a really common feature, not originating from the artifacts of the measurements. The largest difference is shown over the Deccan Peninsula, a dry and elevated plateau where the large annual variation of precipitation and vegetation is evident due to the strong Monsoon.

Figures 3c–3f show respectively the spatial distributions of the skewness and kurtosis of the TOA SW flux distribution from the MISR and CERES observations. The skewness could be reduced from the daily to monthly averages in accord with the central limit theorem, but it still remains strongly positive in the central Southern Pacific. Regions of large positive skewness generally coincide with regions of large positive kurtosis. Very high skewness and kurtosis values concur over the central Southern Pacific ocean which contains less amounts of clouds resulting from less convective activity in the middle of the Intertropical convergence zone (ITCZ) and South Pacific Convergence Zone (SPCZ).

The PDFs of the SW flux show interesting results related to the nature of the flux and the instruments that measure the flux. In Figure 4, the PDFs of the flux over the Deccan Peninsula and central Southern Pacific Ocean clearly show distinct features in each area.

Over the Deccan Peninsula (Figure 4a), the PDFs show a long and thick right tail in both observations. Over the central Southern Pacific ocean (Figure 4b), both PDFs show high skewness and high kurtosis but two observations show differences in the mean and median. The mean and the median of the MISR SW flux are $\sim 6 \text{ W/m}^2$ ($\sim 11\%$) and $\sim 7 \text{ W/m}^2$ ($\sim 14\%$) lower than that of CERES, respectively. The SW flux distributions over this Pacific region are leptokurtic, as they show highly non-Gaussian features with large values of kurtosis about 14 (MISR) and 22 (CERES). The leptokurtic distribution has long tails that asymptotically approach zero more slowly than a Gaussian, therefore producing more outliers than the normal distribution. With higher skewness and kurtosis than the normal distribution, the SW flux has a larger population on the right tail caused by high reflective cloudiness.

Over the high skewness and kurtosis region in the central Southern Pacific Ocean, we find a negative correlation between skewness and SW flux values, as shown in Figure 5. The linear correlation coefficients between skewness and SW flux are -0.72 and -0.73 for MISR and CERES, respectively. Besides, the skewness abruptly increases where the SW flux is less than 60 W/m^2 with relatively less clouds over the Pacific region. We can infer this negative correlation as skewness can be reduced by clouds by their random scattering of the lights. This result corroborates with Datseris and Stevens (2021) that the zonal and temporal distribution of cloud contribution to atmospheric albedo is mostly attributable to the contribution of cloud fraction.

3.2. Seasonal Cycle and Hemispheric Asymmetry of Annual Mean SW

The seasonal cycle of satellite-based global mean albedo and reflected fluxes has been discussed in a number of previous works (Kato, 2009; Stephens et al., 2015, 2016; Song et al., 2018; Datseris & Stevens, 2021; and references therein). What is different about this work from earlier studies is that the zonal and temporal median is

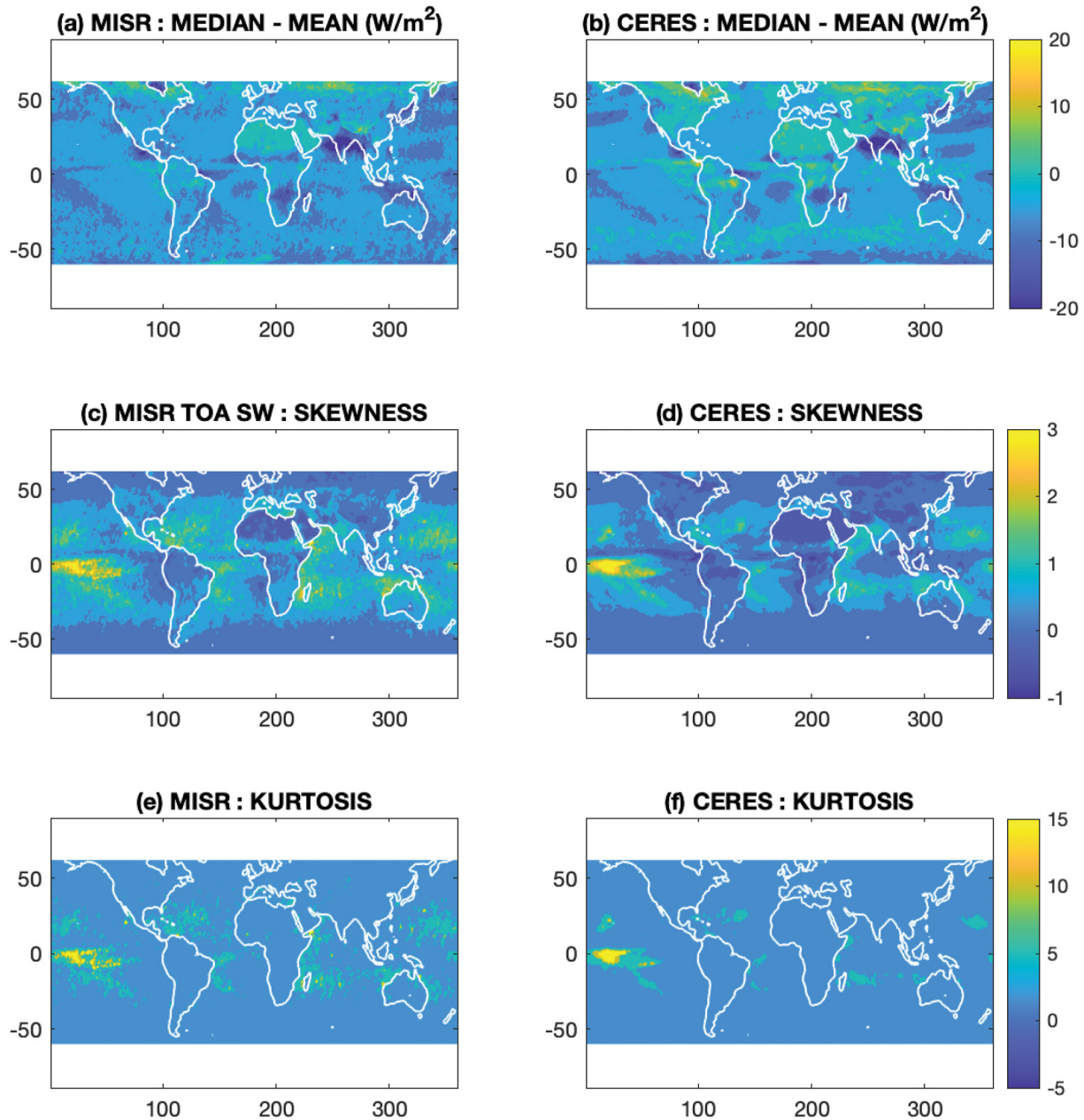


Figure 3. Difference of median and mean climatology of Top of Atmosphere (TOA) shortwave (SW) flux (W/m^2) ((a)–(b)) and spatial distribution of temporal skewness ((c)–(d)) and kurtosis ((e)–(f)) of TOA SW flux from multiangle imaging spectroradiometer and Clouds and the Earth's Radiant Energy System.

also shown beside the temporal average of the zonal mean with MISR and CERES SSF data. The seasonal cycles shown in Figure 6 are the mean and median of 20 annual cycles (2001–2020) from MISR and CERES SSF data on the Terra satellite. Monthly zonal mean and median fluxes are computed from 20 years for each month of the year and the area is weighted and averaged over a given region. The TOA SW flux observations inferred from MISR and CERES produce consistent features of the seasonal cycle of SW flux, as shown in Figure 6.

The seasonal cycle of the SW flux generally follows the seasonal cycle of the solar insolation, based on Sun–Earth distance and inclination angle changes, which determine the local incoming solar insolation at a given time of the year. Strong hemispheric asymmetry is evident that the seasonal cycle amplitude of global mean solar insolation is more than one magnitude smaller (25.3 W/m^2) than those of NH mean (243.9 W/m^2) and SH mean (289.3 W/m^2), when they are calculated with solar insolation appeared in CERES SSF product. The reduced amplitude of the

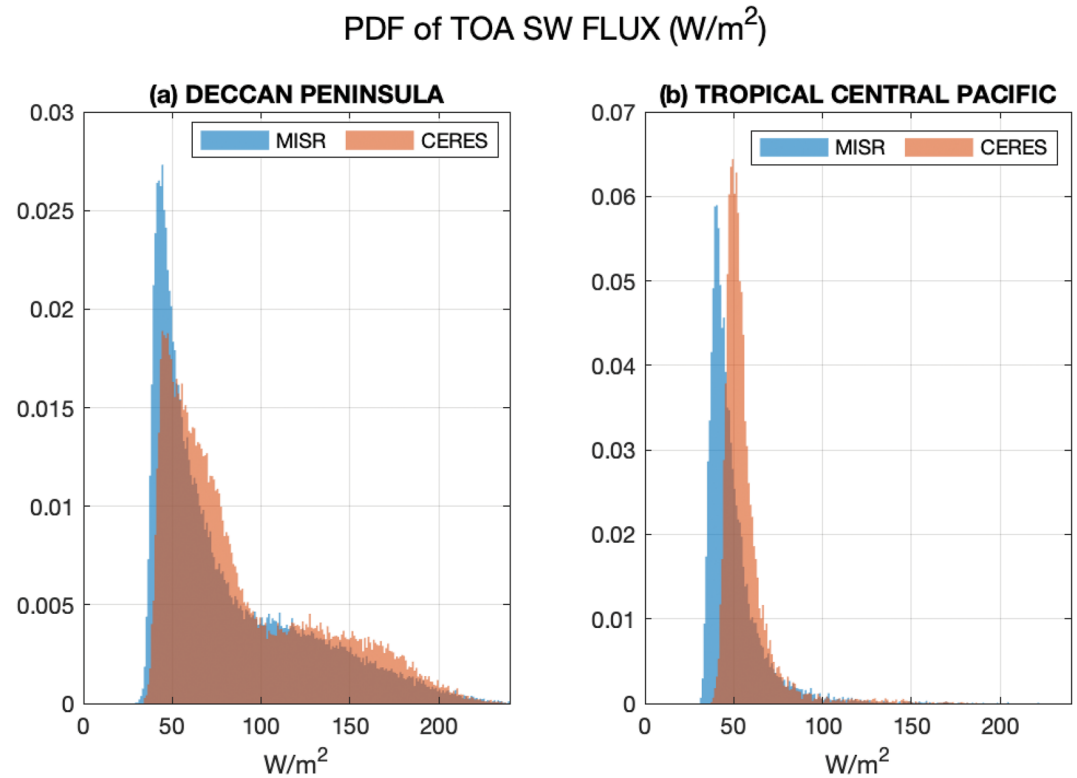


Figure 4. Probability density functions of the shortwave flux over the (a) Deccan Peninsula and (b) central Southern Pacific ocean.

near-global seasonal cycle of SW flux (Figure 6a) compared to that of NH and SH (Figures 6b–6c) illustrates how the hemispheric asymmetry contributes to the global average of the reflected fluxes.

Furthermore, the amount of the reflected SW flux also depends on the atmospheric and surface properties. The global mean SW flux is a combination of the flux over land and ocean, therefore, the seasonal cycle of SW flux is also a combination of land and ocean, depending on the seasonal cycle of cloudiness, vegetation, snow, and ice. The differences between the area-weighted near-global mean and median values (mean - median) are about 3 W/m^2 in both observations due to the over-weighted mean with respect to the median, originating from the positive skewness.

The amplitudes of the annual cycle over the ocean (Figures 6h–6i) are larger than those over land (Figures 6e–6f) in both hemispheres. The seasonal cycle of land surface albedo has a summertime minimum resulting from the vegetation and a wintertime maximum resulting from the brighter snow-covered lands. In both land and ocean cases, the amplitudes of the annual cycle in the SH (Figures 6f–6i) are $\sim 20 \text{ W/m}^2$ greater than those in the NH. The large amplitude of the annual cycle over the SH ocean (Figure 6i) can be attributed to the reflection from midlatitude clouds over the storm track during the austral winter.

Despite the strong seasonal variations in the reflected SW flux, the annual means for the NH and SH are nearly equal. Whether this is accidental or intrinsic to the Earth's climate system or variable with time is subject to research debate (Datseris & Stevens, 2021). Different from earlier studies with CERES EBAF SW flux, we analyzed the CERES Terra, Aqua, and

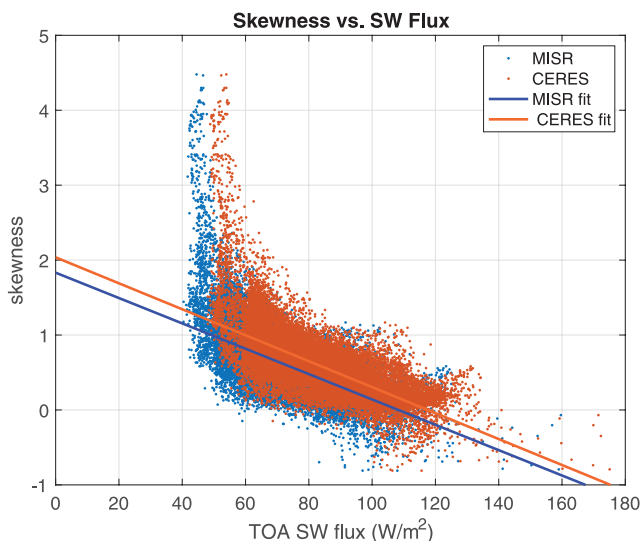


Figure 5. Scatter plot of skewness of the Top of Atmosphere (TOA) shortwave (SW) flux with respect to the TOA SW flux values over the high skewness area in the central Southern Pacific ocean.

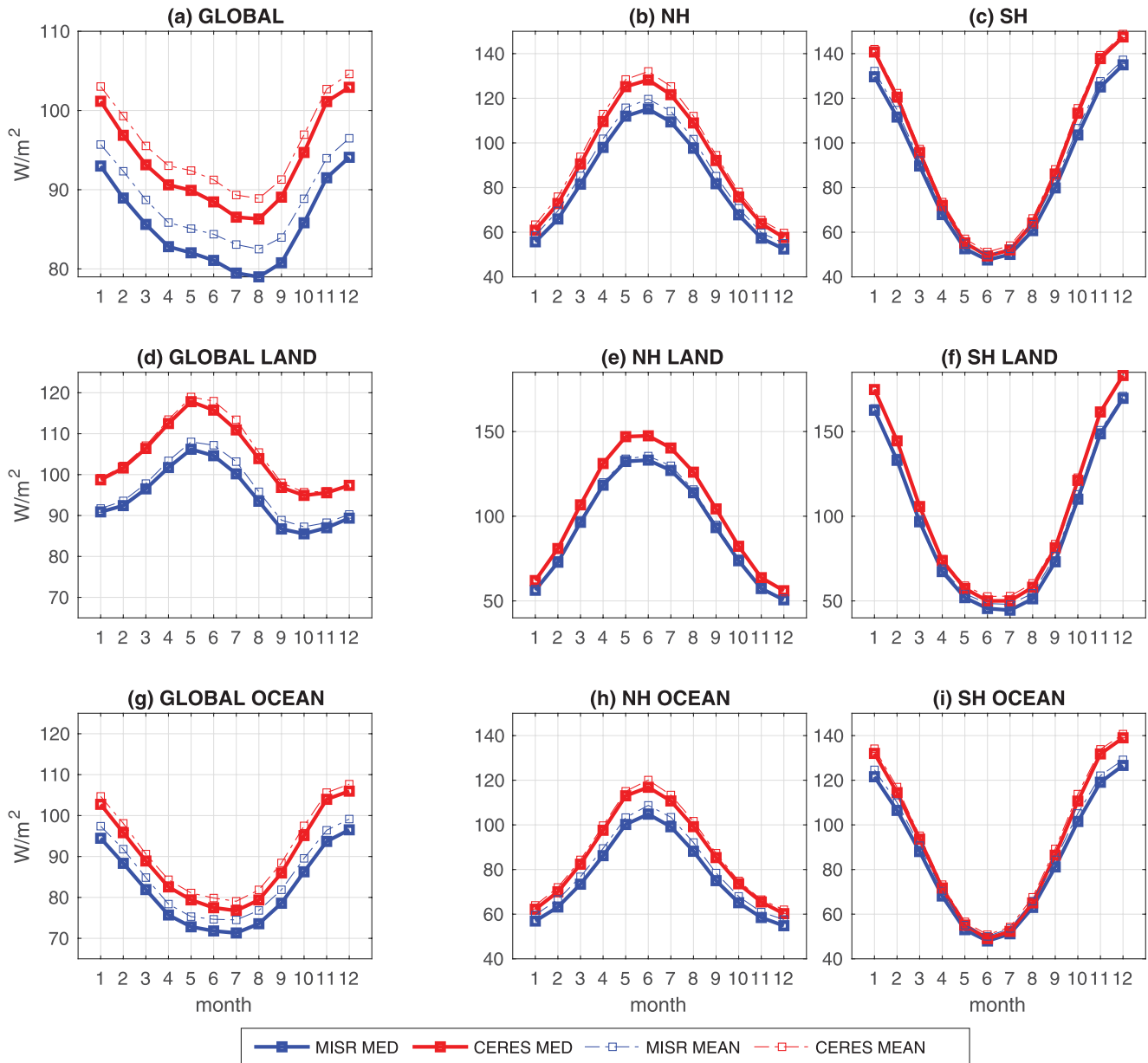


Figure 6. Annual cycles of the mean and median climatology of the shortwave flux (W/m^2) from multiangle imaging spectroradiometer and Clouds and the Earth's Radiant Energy System for near-global (left), NH (center), and SH (right). The second and third rows are NH and SH land and ocean, respectively. The filled marks represent median values of the fluxes and unfilled marks represent mean of the fluxes.

EBAF data separately. Annually averaged TOA SW flux (W/m^2) during 2001–2020 is summarized in Table 1 at a given region.

For the Terra-only MISR and CERES SW flux, observed at $\sim 10:30$ a.m. local time, the hemispheric asymmetry is evident that the SH reflects 3.92 and 1.15 W/m^2 more mean SW flux than the NH, respectively. For the Aqua-only CERES SW flux, obtained at $\sim 1:30$ p.m. local time, the hemispheric asymmetry has the opposite sign, which largely offsets the SH–NH difference in Terra flux to produce a nearly equal TOA SW flux in both hemispheres.

The hemispheric symmetry in the annual and long-term mean TOA SW flux has a significant implication for Earth's energy balance, as any inequality would require compensation from the LW flux or inter-hemispheric energy transfers (e.g., meridional oceanic heat transfer). Compared to the NH, the SH has much more ocean

Table 1

Annual Mean TOA Reflected SW Flux (W/m^2) From 2001 to 2020 for Different Regions From MISR, CERES SSF, and CERES EBAF Products

	MISR (W/m^2)	CERES SSF (W/m^2)	CERES SSF (W/m^2)	CERES EBAF (W/m^2)
	(80S-80 N)	(80S-80 N)	(90S-90 N)	(90S-90 N)
Global	88.41 (85.34)	95.68 (93.40)	96.26 (93.98)	99.04 (96.92)
NH	86.43 (82.88)	95.11 (92.26)	95.53 (92.67)	98.94 (96.29)
SH	90.35 (87.76)	96.26 (94.52)	96.99 (95.27)	99.14 (97.54)
SH - NH	3.92 (4.89)	1.15 (2.26)	1.47 (2.60)	0.20 (1.60)
LAND	96.26 (94.55)	105.37 (104.35)	105.38 (104.37)	110.36 (109.52)
OCEAN	85.05 (82.08)	91.56 (89.51)	91.59 (89.53)	94.21 (92.18)
NH LAND	95.21 (93.76)	104.89 (103.98)	104.90 (103.99)	108.18 (107.31)
SH LAND	98.45 (96.19)	106.36 (105.16)	105.14 (104.90)	114.87 (114.10)
NH OCEAN	80.40 (77.12)	88.39 (86.38)	88.44 (86.44)	92.59 (90.62)
SH OCEAN	88.42 (85.66)	93.84 (91.76)	93.86 (91.77)	95.38 (93.31)

Note. Numbers in parenthesis are calculated with zonal median, instead of zonal mean.

which is less reflective than land, so the SH is expected to reflect less than the NH. However, the hemispheric symmetry of the SW flux with an equal amount of reflected flux in each hemisphere has been reported and explained by increased SH clouds offsetting the greater reflection from the NH land masses. We can infer that this is offsetting by morning clouds, measured at 10:30 a.m. local time overwhelms the effect of hemispheric imbalance of land and ocean masses between two hemispheres. The marine stratocumulus has a maximum thickness during the morning and a minimum thickness during the afternoon, which is an important control of the diurnal cycle of global outgoing SW flux (Gristey, Chiu, et al., 2018; Gristey, Su, et al., 2018). We can speculate that the high SW flux in the SH from the Terra observation is due to the thick morning marine stratocumulus since this type of cloud is more widespread in the SH than in the NH. Similarly, less SW is reflected in the SH, by the time of the Aqua overpass in the afternoon when those clouds have dissipated. More details on the difference between NH and SH are further discussed in the discussions section.

3.3. Height-Dependent CERES-MISR Differences

The multi-year (2001–2020) TOA SW median climatology from MISR and CERES agree fairly well with each other over non-polar regions, with the bias close to 7 W/m^2 and the RMS error of 8.5 W/m^2 . As shown in Figure 7, the differences, CERES - MISR, are in general positive everywhere except Greenland and SH high latitude regions, since the near-global mean TOA SW flux from CERES is close to 7 W/m^2 greater than that from MISR. Black and red contour lines in the figure indicate high elevation areas ($z > 2 \text{ km}$) and high cloud regions (cloud height $> 9 \text{ km}$), respectively.

It is interesting that the largest differences up to 30 W/m^2 are observed over tropical high cloud regions where monthly mean cloud top heights are higher than 9 km . Regions where the elevation is higher than 2 km also show large differences. The cloud top heights are acquired from the same CERES SSF product. The world terrain reference (World Geodetic System, 1984) model is used in this study, which is the same data set used by the Terra MISR and CERES algorithms.

While TOA SW flux inferred from multiple directions is ideally expected to be independent of satellite viewing geometry by definition, two fluxes from multiple directions over the same scene are not identical due to differences in geometry and algorithm. Differences between the two measurements indicate that there exist uncertainties in spatial and temporal matching, narrow-to broadband conversion, parallax effects, and algorithms for the angular corrections of the radiance field. Each instrument's algorithms, MISR's Bidirectional Reflectance Factor (BDF) corrections and CERES ADMs, account for the angular distribution of the radiance, which is strongly dependent on the physical and optical properties of each scene for a given surface type, cloud fraction, cloud/aerosol optical depth, cloud phase, as well as the illumination angle (Loeb et al., 2006).

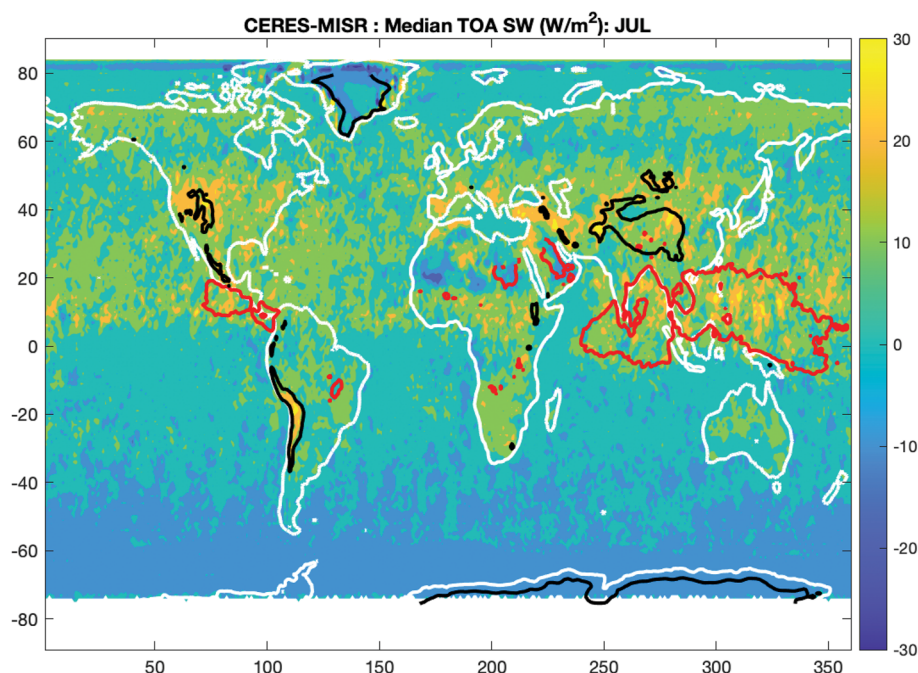


Figure 7. Differences of median climatology (2001–2020) of Top of Atmosphere shortwave flux (W/m^2) between multiangle imaging spectroradiometer and Clouds and the Earth's Radiant Energy System from the Terra satellite. Black and red contour lines indicate high elevation area ($z > 2$ km) and high cloud regions (cloud height > 9 km), respectively.

The uncertainties of the TOA albedos from CERES and MISR have been carefully estimated in previous works. Over the overcast ocean scenes within 75S–75 N, the uncertainty in the MISR albedos due to narrow-to-broad band albedo conversion is $\sim 2\%$ (Sun et al., 2006). Similarly, the difference between the MISR and CERES albedos due to the angular distribution model (ADM) is estimated to be $\sim 4\%$. Over the Arctic overcast scene, the difference between the two measured albedos is mostly due to differential BRDF anisotropic corrections, and it is estimated to be less than 4% when the solar zenith angle (SZA) is less than 70° , while it increases up to 13.5% when the SZA is greater than 80° (Zhan et al., 2018).

We further classified the PDFs of MISR and CERES SW flux (W/m^2) over the ocean (60S–60 N) for different cloud heights from 1 to 12 km, as shown in Figure 8. As the cloud heights increase, the difference between the two observations grows. Besides, the PDFs are getting close to the normal distribution, and the skewness approaches zero over high cloud regions. This is also shown in a graph of the difference between CERES and MISR (%) and the skewness of the PDFs as a function of cloud heights (Figure 9).

Besides the cloud properties, that is, cloud fraction, optical depth, and phase of clouds, the magnitude of the SW also depends on the three-dimensional (3D) structure of clouds (Ham et al., 2015; Singer et al., 2021). The effects of 3D cloud morphology on SW reflectance, which are not fully resolved in the radiative transfer algorithm, may cause additional bias in two measurements for high cloud scenes.

4. Discussions

4.1. Hemispheric Asymmetry in SW Flux

Diurnal sampling plays an important role in the hemispheric asymmetry, and SH–NH differences, of the TOA SW flux. As reported in the previous section, this difference is positive in the Terra observations (i.e., MISR and CERES), but negative in the Aqua CERES. As shown in Figure 10, the CERES EBAF result is approximately the average of the Terra and Aqua observation, while different SW flux data show a similar interannual variation. To assess the degree to which the hemispheric symmetry is sensitive to the missing coverage at high latitudes, we compared the annual mean EBAF CERES SW fluxes with various missing portions of high-latitude coverage. Although the interannual variations tend to track each other, the SH–NH differences are relatively small for the

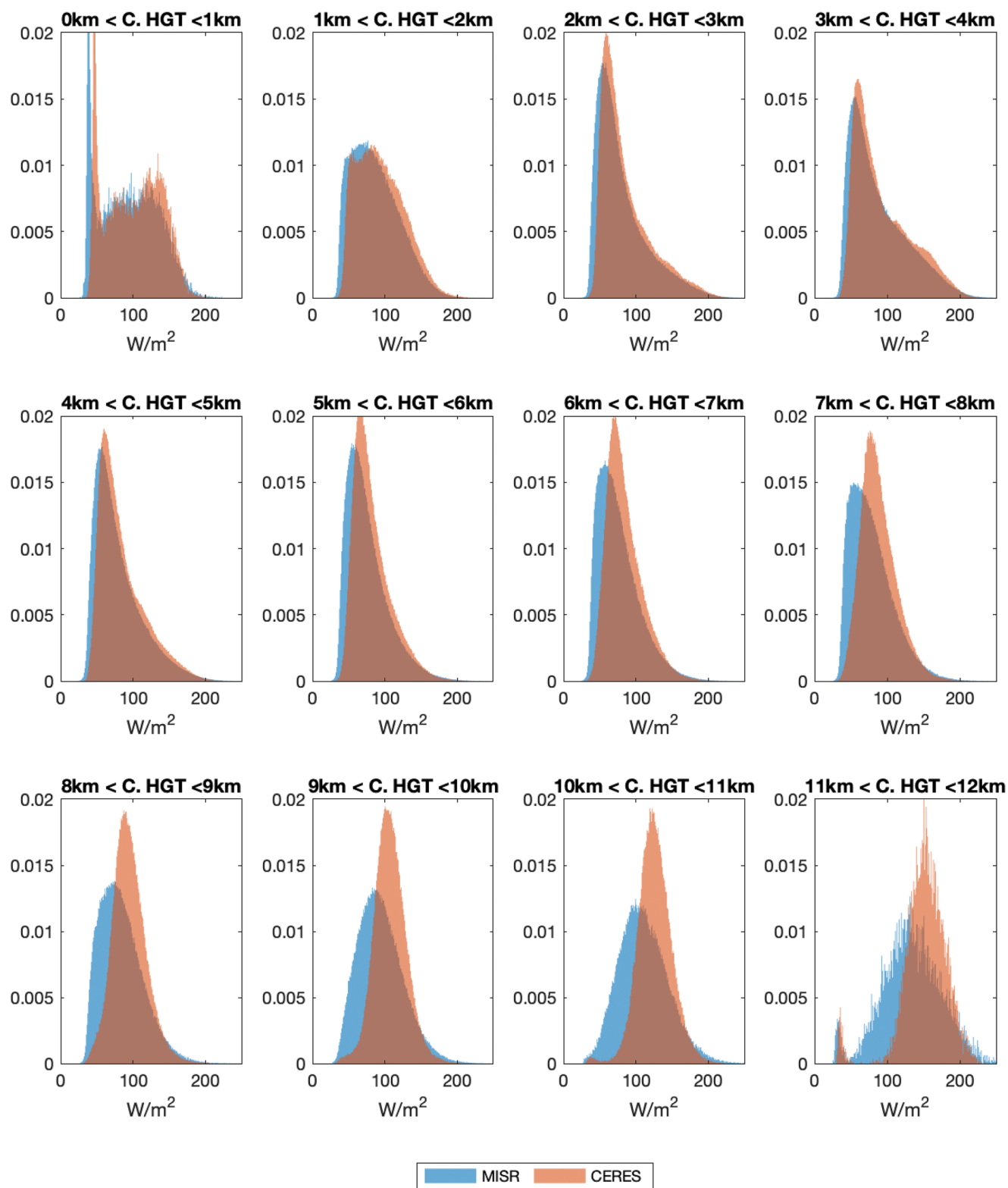


Figure 8. Probability density functions of multiangle imaging spectroradiometer and Clouds and the Earth's Radiant Energy System shortwave flux (W/m^2) over the ocean for different cloud heights from 1 to 12 km.

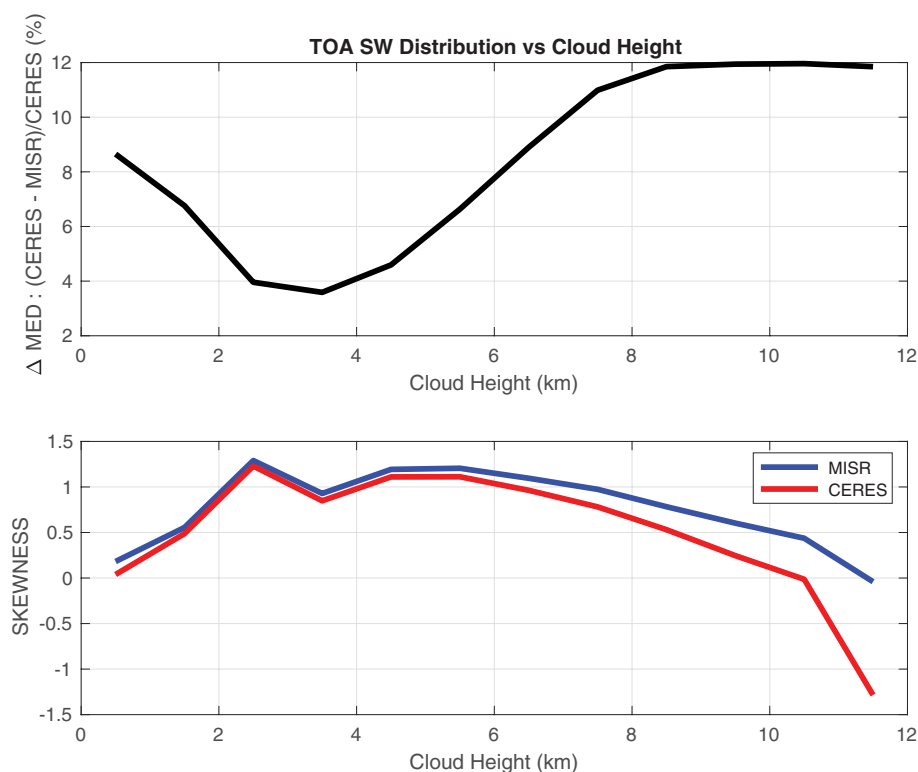


Figure 9. The difference between two median values (Clouds and the Earth's Radiant Energy System [CERES] - multiangle imaging spectroradiometer)/CERES in % and skewness of the Top of Atmosphere shortwave distribution over the ocean, as a function of cloud height.

global averages with missing latitudes 70° poleward. But the differences start to increase as more polar latitudes are not covered. For example, if the coverage misses 60° poleward, the SH-NH differences can be $\sim 2 \text{ W/m}^2$ with the SH flux being lower, largely because of the extensive coverage from clouds and Antarctic ice. From this analysis, we concluded that the missing latitude coverage cannot explain the large difference between MISR and CERES observations from Terra. The MISR-CERES difference is likely due to the underlying assumptions used in their algorithms. For MISR, it requires to convert four narrow-band fluxes to obtain the broadband SW flux, although it measures these narrow-band fluxes from multiple angles along the orbital track. On the other hand, CERES needs to convert the broad-band radiance from a single scan to the full hemispheric SW flux, which requires knowledge of angular distribution models (ADMs) for each scene. In both MISR and CERES SW retrievals, scene type classification is required to carry out the narrow-to-broad-band (MISR) and radiance-to-flux (CERES) conversion.

Characteristics of the Terra and Aqua CERES sampling are described in Figure 11 in which the NH and SH exhibit very different local time coverages. Thus, the diurnal variations of TOA SW are critical for understanding and interpreting the hemispheric symmetry. If the SW diurnal variation is symmetric at about noon, the average of Terra and Aqua data would yield cancellation of the SH-NH asymmetric values observed by each satellite alone. However, if the diurnal variation is not symmetric with respect to noon, their average would not cancel the SH-NH differences. A recent study showed that the SW diurnal variation from the CERES EBAF is somewhat different from the one inferred from the DSCOVR/EPIC observation (Lim et al., 2021). In addition, the rate of daytime cloud fraction changes from DSCOVR/EPIC observations is not symmetric about noon either (Delgado-Bonal et al., 2021). The diurnal variation of albedo estimated from the Earth Radiation Budget Experiment (ERBE) also shows that the albedo variations are not always symmetric with respect to noon due to variations of cloudiness throughout the day, which are asymmetric about noon (Rutan et al., 2014). The diurnal variations built in CERES EBAF are largely based on geostationary satellite observations, which cover latitudes up to 60° N/S. Therefore, the uncertainty is likely high in the CERES EBAF data for the SW diurnal variation 60° poleward. This is the region where the Terra and Aqua local time samplings differ most, as shown in Figure 11.

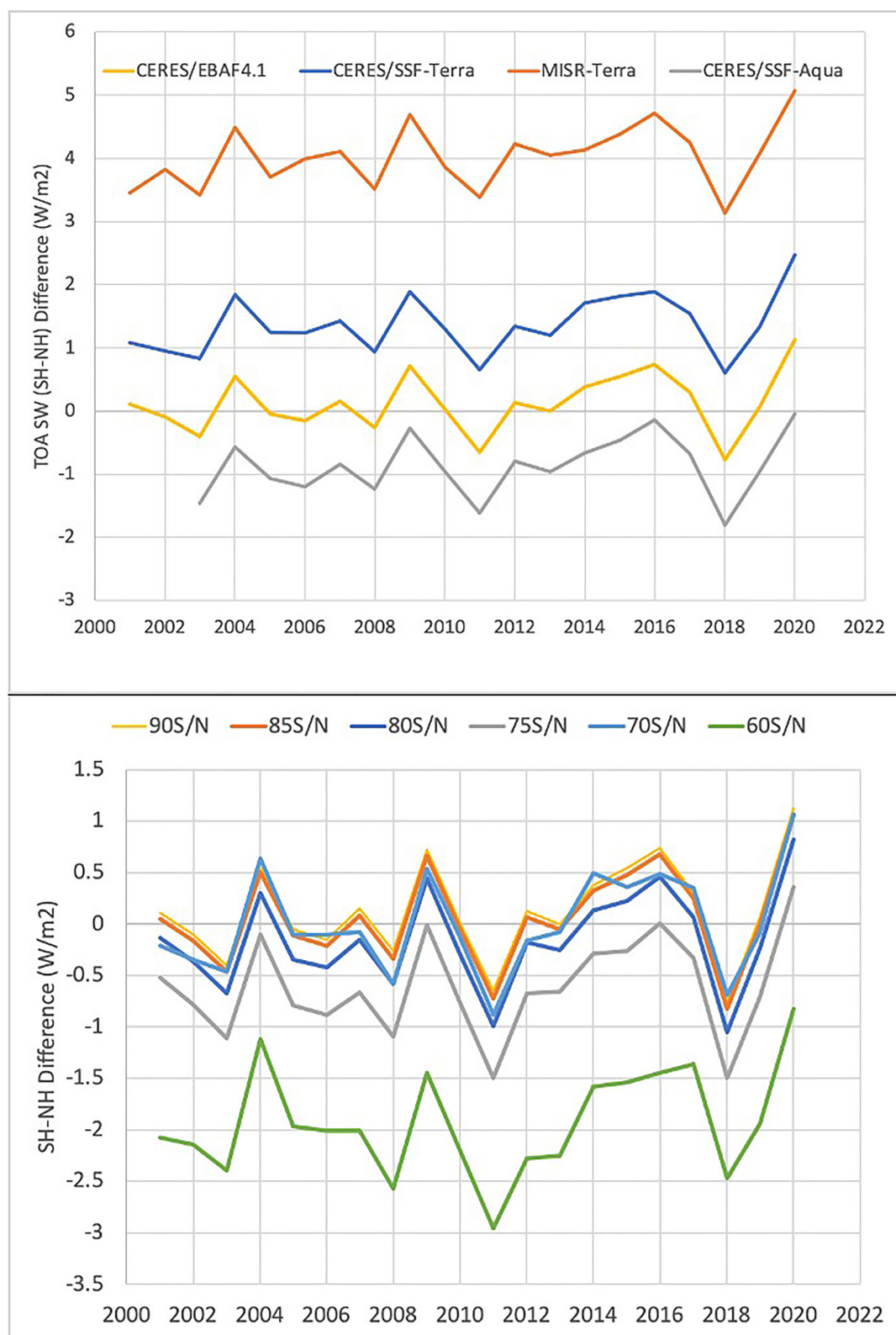


Figure 10. Time series of annual mean NH and SH Top of Atmosphere shortwave (TOA SW) fluxes from Clouds and the Earth's Radiant Energy System (CERES) energy balanced and filled (EBAF), CERES-Terra, CERES-Aqua, and multiangle imaging spectroradiometer-Terra (upper) and CERES EBAF TOA SW flux differences with various missing latitudes (lower). The poleward missing latitudes are indicated by the plot legend.

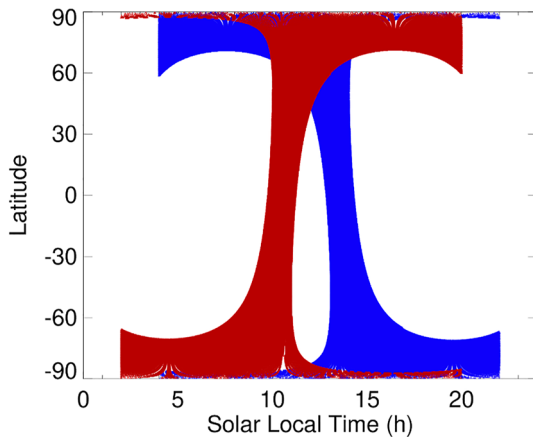


Figure 11. Local time coverage from Terra (red) and Aqua (blue) Clouds and the Earth's Radiant Energy System. 1 Jan 2008 is used to illustrate the differences between the NH and SH sampling in local time.

Our analysis result stresses the importance of diurnal sampling for the SW observations from future missions. Potential constellations of the satellite observations have been suggested to better resolve distinct diurnal signatures of the outgoing Earth radiation (Gristey et al., 2017; Hakuba et al., 2019; Mefta et al., 2021; Swartz et al., 2019). As a continuation mission to CERES, NASA's Libera (<https://lasp.colorado.edu/home/libera/>) is planned to fly on the Joint Polar Satellite System-3 (JPSS-3) satellite (1:30 p.m. equator-crossing time) to maintain the long-term record of TOA radiative fluxes. The Libera's sampling will be similar to Aqua and would require a diurnal cycle model to obtain the daytime mean TOA SW flux. Without correcting the diurnal variation, Libera's SH-NH difference would be similar to Aqua CERES observations seen in Figure 11.

4.2. Possible Causes of the TOA SW Skewness Variations

We show that monthly mean TOA SW fluxes are obviously not normally distributed but positively skewed as a mixture of fluxes from land and ocean. According to the central limit theorem, the average of many observations of a random variable approaches a normal distribution. However, in the case of

TOA SW observation, the normality of the distribution is not acquired by taking an average for the monthly mean from the daily means. Actually, the PDFs of daily mean and monthly mean flux show similar skewed features. On a global scale, the PDFs of SW flux are relatively thick in the left tail, because there exists a low boundary of zero reflectance when they do not get solar insolation during the polar nights. There also exists extreme high SW flux values above 400 W/m^2 over the summer polar regions.

The skewness of the SW flux distribution is not globally uniform, but changes depending on the selection of the spatial and temporal sampling. Besides, the large positive skewness of the observed TOA SW tends to occur in the extreme climatic regions where the seasonal variation of SW flux is relatively high. The PDF of the flux changes with the season of the year, as the mean of the flux, shows substantial seasonal variations (Figure 6) following the changes in the vegetation, clouds, ice, and atmospheric conditions. For example, the summertime PDF of the flux over land is quite different from the wintertime distribution (not shown) and the PDF over the land is different from that over the ocean. While the negative skewness is often shown over the low-to the mid-latitude arid area over the African continent, the positive skewness is generally appeared over the ocean, as can be seen in Figures 3c–3d.

The PDFs of SW flux over high cloud regions are less skewed, compared to those over low cloud regions (Figures 8 and 9). Because the interannual variations in SW skewness are derived from variations of clouds, they are sensitive to the outlier years when the flux behaves abnormally, such as those from a strong ENSO event. Skewness often becomes significant in cases where data variability has a lower or upper boundary. The data with a lower bound tend to have positive skewness while the data with an upper bound are often skewed left. In the central Southern Pacific, where the annual mean CERES SWs are lowest and mostly from a clear sky, the skewness is positively high. This is the region influenced strongly by the downward branch of both Hadley and Walker circulations on an annual basis and is apparently sensitive to ENSO-induced circulation changes.

The skewness of the TOA SW flux seems to have originated from multiple sources. Regionally, the variations of clouds due to ENSO and Monsoon can generate significant skewness. However, seasonal variation can create skewness even in high latitudes where the ENSO and Monsoon variations are relatively weak. A comparison of the TOA SW flux from MISR and CERES shows that the measurement artifacts could also generate different skewnesses over high cloud regions. In the first order, the PDF of the global SW flux is a combination of PDFs from land and ocean. Combining two or more Gaussian distributions with different means and standard deviations can generate the non-Gaussian distribution. Furthermore, neither SW flux at grids over land nor at grids over the ocean show a normal distribution.

The non-Gaussian feature of the incoming total solar insolation (TSI) (skewness = -0.13 ; kurtosis = 0.13) can also potentially contribute to the skewness of the reflected flux. The amplitude of the Solar Radiation and Climate Experiment (SORCE) measured TSI variation, $\delta(\text{TSI})$, is less than 1 W/m^2 during the whole measurement period

(2003–2020). The maximum uncertainty of the TOA incoming solar flux estimated from the TSI variation, $\delta S_0 = \delta(TSI)/4$, is $\sim 0.25 \text{ W/m}^2$. However, the effect of the total energy variation on the distribution of the incident solar insolation at a given time and location of the Earth should be considered in future studies, as suggested by Datseris and Stevens (2021).

5. Conclusions

The 20-year observations from MISR and CERES offer an excellent opportunity to characterize their similarities and differences in these independently derived TOA SW flux data sets from the same Terra platform. The analysis presented in this paper can be summarized in the following:

1. The PDFs of MISR and CERES SW fluxes commonly show that the TOA SW flux is not normally distributed but positively skewed. Distinct PDFs of the TOA SW flux can impact the quantification of the globally averaged flux. In both observations, the near-global median value of the SW flux is $\sim 3 \text{ W/m}^2$ less than the mean of the flux, due to the positive skewness of the SW flux distribution. The near-global mean TOA SW flux converted from MISR narrow bands albedo is about 7 W/m^2 ($< 7\%$) less than CERES measured flux during the last two decades. Gaussian distributions are naturally assumed in atmospheric data analysis, as the central limit theorem states that distributions of random variables approach a normal distribution by taking their mean. This, however, is not always true for the TOA SW flux distribution. The PDFs of SW flux are relatively thick in the left tail because there exists a low boundary of zero reflectance when they do not get solar insolation during the polar nights.
2. From Terra's AM observation ($\sim 10:30 \text{ a.m.}$ local time), SH reflects ~ 1 and $\sim 4 \text{ W/m}^2$ more SW flux than NH, with MISR and CERES SSF1deg product, respectively. Hemispheric mean SW flux depends on the time of satellite measurement since diurnal sampling plays an important role in the determination of the daily mean. Different local time coverage in Terra and Aqua observation can cause sampling bias in estimating SW flux climatology in both hemispheres.
3. While the characteristics of the two SW fluxes broadly agree with each other, differences in the regional PDF from two different SW fluxes are substantially significant over high cloud regions and high altitude regions. Our analysis shows that some parts of the different skewness from the two measurements may be attributed to different treatments of the radiance anisotropy over high cloud scenes. More analysis based on the spatially and temporally collocated merged data set of CERES/MISR radiances (Loeb et al., 2006; Su et al., 2015a, 2015b; Zhan et al., 2018) and TOA albedo observed from Advanced Very High-Resolution Radiometer (Zhan & Liang, 2022) will further help to check the consistencies and uncertainties of the TOA SW flux measurements from the different instruments and to direct to the potential areas requiring improved solutions. The significant variations in incoming SW flux could be hampering signal detection for the controlling mechanism of the TOA SW flux. Further analysis of TOA albedo and spectral albedo should therefore be considered in future work.

Data Availability Statement

Observed data supporting the findings of this article are available online and should be cited as Doelling (2015) [Data set], Doelling (2019) [Data set], and Diner (2009) [Data set]. All data are available from <https://ceres-tool.larc.nasa.gov/ord-tool/jsp/SSF1degEd41Selection.jsp>, <https://ceres.larc.nasa.gov/data/#ebaftoa-level-3>, and <https://asdc.larc.nasa.gov/documents/misr/version/pge12b.html>.

Acknowledgments

We thank the MISR and CERES Science Team for making the TOA albedo and SW flux data available on their websites, and three anonymous reviewers for their suggestions that helped to improve this manuscript. This work is supported by NASA's Sun-Climate research at Goddard Space Flight Center.

References

- Barker, H. W., Wiellicki, B. A., & Parker, L. (1996). A parameterization for computing grid-averaged solar fluxes for inhomogeneous marine boundary layer clouds. Part II: Validation using satellite data. *Journal of Atmospheric Sciences*, 53(16), 2304–2316. [https://doi.org/10.1175/1520-0469\(1996\)053<2304:apfcga>2.0.co;2](https://doi.org/10.1175/1520-0469(1996)053<2304:apfcga>2.0.co;2)
- Datseris, G., & Stevens, B. (2021). Earth's albedo and its symmetry. *AGU Advances*, 2, e2021AV000440. <https://doi.org/10.1029/2021AV000440>
- Delgado-Bonal, A., Marshak, A., Yang, Y., & Oreopoulos, L. (2021). Global daytime variability of clouds from DSCOVR/EPIC observations. *Geophysical Research Letters*, 48, e2020GL091511. <https://doi.org/10.1029/2020GL091511>
- Diner, D. (2009). MISR Level 3 Component Global Albedo product in netCDF format covering a day - Version 6. [Data set]. NASA Langley Atmospheric Science Data Center DAAC. https://doi.org/10.5067/TERRA/MISR/MIL3DALN_L3.006

- Diner, D. J., Beckert, J. C., Reilly, T. H., Bruegge, C. J., Conel, J. E., Kahn, R. A., et al. (1998). Multi-angle imaging spectroRadiometer (MISR) instrument description and experiment overview. *IEEE Transactions of the Geosciences and Remote Sensing*, 36, 1072–1087. <https://doi.org/10.1109/36.700992>
- Diner, D. J., Braswell, B. H., Davies, R., Gobron, N., Hu, J., Jin, Y., et al. (2005). The value of multiangle measurements for retrieving structurally and radiatively consistent properties of clouds, aerosols, and surfaces. *Remote Sensing of Environment*, 97, 495–518. <https://doi.org/10.1016/j.rse.2005.06.006>
- Doelling, D. (2015). CERES Level 3 SSF1deg-Month Terra-MODIS HDF file - Edition 4A. [Data set]. NASA Langley Atmospheric Science Data Center DAAC. https://doi.org/10.5067/TERRA/CERES/SSF1DEGMONTH_L3.004A
- Doelling, D. (2019). CERES Energy Balanced and Filled (EBAF) TOA and Surface Monthly means data in netCDF Edition 4.1. [Data set]. NASA Langley Atmospheric Science Data Center DAAC. https://doi.org/10.5067/TERRA-AQUA/CERES/EBAF_L3B.004.1
- Doelling, D. R., Loeb, N. G., Keyes, D. F., Nordeen, M. L., Morstad, D., Nguyen, C., et al. (2013). Geostationary enhanced temporal interpolation for CERES flux products. *Journal of Atmospheric and Oceanic Technology*, 30(6), 1072–1090. <https://doi.org/10.1175/JTECH-D-12-00136.1>
- Feller, W. (1971). *An introduction to probability theory and its applications*, 2nd Edn, (Vol. 2). Wiley.
- Gristey, J. J., Chiu, J. C., Gurney, R. J., Han, S.-C., & Morcrette, C. J. (2017). Determination of global Earth outgoing radiation at high temporal resolution using a theoretical constellation of satellites. *Journal of Geophysical Research: Atmospheres*, 122, 1114–1131. <https://doi.org/10.1002/2016JD025514>
- Gristey, J. J., Chiu, J. C., Gurney, R. J., Morcrette, C. J., Hill, P. G., Russell, J. E., & Brindley, H. E., (2018). Insights into the diurnal cycle of global Earth outgoing radiation using a numerical weather prediction model. *Atmospheric Chemistry and Physics*, 18, 5129–5145. <https://doi.org/10.5194/acp-18-5129-2018>
- Gristey, J. J., Su, W., Loeb, N. G., Vonder Haar, T. H., Tornow, F., Schmidt, K. S., et al. (2018). Shortwave radiance to irradiance conversion for Earth radiation budget satellite observations: A review. *Remote Sensing*, 13(13), 2640
- Gristey, J. J., Su, W., Loeb, N. G., Vonder Haar, T. H., Tornow, F., Schmidt, K. S., et al. (2021). Shortwave radiance to irradiance conversion for Earth radiation budget satellite observations: A review. *Remote Sensing*, 13(13), 2640. <https://doi.org/10.3390/rs13132640>
- Hakuba, M. Z., Stephens, G. L., Christophe, B., Nash, A. E., Foulon, B., Bettadpur, S. V., et al. (2019). Earth's energy imbalance measured from space. *IEEE Transaction and Geosciences Remote Sensing*, 57(1), 32–45. <https://doi.org/10.1109/TGRS.2018.2851976>
- Ham, S.-H., Kato, S., Barker, H. W., Rose, F. G., & Sun-Mack, S. (2015). Improving the modelling of short-wave radiation through the use of a 3D scene construction algorithm. *Quarterly Journal of the Royal Meteorological Society*, 141, 1870–1883. <https://doi.org/10.1002/qj.2491>
- Kato, S. (2005). Top-of-atmosphere shortwave broadband observed radiance and estimated irradiance over polar regions from Clouds and the Earth's Radiant Energy System (CERES) instruments on Terra. *Journal of Geophysical Research*, 110(D7), D07202. <https://doi.org/10.1029/2004JD005308>
- Kato, S. (2009). Interannual variability of the global radiation budget. *Journal of Climate*, 22(18), 4893–4907. <https://doi.org/10.1175/2009jcli2795.1>
- Kopp, G., & Lean, J. L. (2011). A new, lower value of total solar irradiance: Evidence and climate significance. *Geophysical Research Letters*, 38, L01706. <https://doi.org/10.1029/2010GL045777>
- L'Ecuier, T. S. (2017). Earth's energy balance. In *International Encyclopedia of Geography: People, the Earth, Environment and Technology*. <https://doi.org/10.1002/9781118786352.wbieg1132>
- Lim, Y.-K., Wu, D. L., Kim, K.-M., & Lee, J. N. (2021). An investigation on seasonal and diurnal cycles of TOA shortwave radiations from DSCOVR/EPIC, CERES, MERRA-2, and ERA5. *Remote Sensing*, 13, 4595. <https://doi.org/10.3390/rs13224595>
- Loeb, N. G., Doelling, D. R., Wang, H., Su, W., Nguyen, C., Corbett, J. G., et al. (2018). Clouds and the Earth's radiant energy system (CERES) energy balanced and filled (EBAF) top-of-atmosphere (TOA) Edition-4.0 data product. *Journal of Climate*, 31(2), 895–918. <https://doi.org/10.1175/JCLI-D-17-0208.1>
- Loeb, N. G., Kato, S., Loukachine, K., & Manalo-Smith, N. (2005). Angular distribution models for top-of-atmosphere radiative flux estimation from the clouds and the Earth's radiant energy system instrument on the Terra satellite. Part I: Methodology. *Journal of Atmospheric and Oceanic Technology*, 22, 338–351. <https://doi.org/10.1175/JTECH1712.1>
- Loeb, N. G., Kato, S., Loukachine, K., & Manalo-Smith, N. (2007). Angular distribution models for top-of-atmosphere radiative flux estimation from the clouds and the Earth's radiant energy system instrument on the Terra satellite. Part II: Validation. *Journal of Atmospheric and Oceanic Technology*, 24, 564–584. <https://doi.org/10.1175/JTECH1983.1>
- Loeb, N. G., Sun, W., Miller, W. F., Loukachine, K., & Davies, R. (2006). Fusion of CERES, MISR, and MODIS measurements for top-of-atmosphere radiative flux validation. *Journal of Geophysical Research*, 111, D18209. <https://doi.org/10.1029/2006JD007146>
- Loeb, N. G., & Wielicki, B. A. (2015). *Satellites and Satellite Remote Sensing | Earth's radiation Budget, Encyclopedia of atmospheric Sciences* (2nd ed.), (pp. 67–76). Academic Press. <https://doi.org/10.1016/B978-0-12-382225-3.00349-2>
- Loeb, N. G., Wielicki, B. A., Doelling, D. R., Smith, G. L., Keyes, D. F., Kato, S., et al. (2009). Toward optimal closure of the Earth's top-of-atmosphere radiation budget. *Journal of Climate*, 22(3), 748–766. <https://doi.org/10.1175/2008jcli2637.1>
- Meftah, M., Boutéraon, T., Dufour, C., Hauchecorne, A., Keckhut, P., Finance, A., et al. (2021). The UVSQ-SAT/INSPIRESat-5 CubeSat mission: First in-orbit measurements of the Earth's outgoing radiation. *Remote Sensing*, 13(8), 1449. <https://doi.org/10.3390/rs13081449>
- Rutan, D. A., Smith, G. L., & Wong, T. (2014). Diurnal variations of albedo retrieved from Earth radiation budget experiment measurements. *Journal of Applied Meteorology and Climate*, 53(12), 2747–2760. <https://doi.org/10.1175/jamc-d-13-0119.1>
- Sardeshmukh, P. D., Compo, G. P., & Penland, C. (2015). Need for caution in interpreting extreme weather statistics. *Journal of Climate*, 28(23), 9166–9187. <https://doi.org/10.1175/JCLI-D-15-0020.1>
- Singer, C. E., Lopez-Gomez, I., Zhang, X., & Schneider, T. (2021). Top-of-Atmosphere albedo bias from neglecting three-dimensional cloud radiative effects. *Journal of the Atmospheric Sciences*, 78(12), 4053–4069.
- Song, Z., Liang, S., Wang, D., Zhou, Y., & Jia, A. (2018). Long-term record of top-of-atmosphere albedo over land generated from AVHRR data. *Remote Sensing of Environment*, 211, 71–88. <https://doi.org/10.1016/j.rse.2018.03.044>
- Stephens, G., Li, J., Wild, M., Clayson, C. A., Loeb, N., Kato, S., et al. (2012). An update on Earth's energy balance in light of the latest global observations. *Nature Geosciences*, 5, 691–696. <https://doi.org/10.1038/ngeo1580>
- Stephens, G. L., Hakuba, M. Z., Hawcroft, M., Haywood, J. M., Behrang, A., Kay, J. E., & Webster, P. J. (2016). The curious nature of the hemispheric symmetry of the Earth's water and energy balances. *Current Climate Change Reports*, 2(4), 135–147. <https://doi.org/10.1007/s40641-016-0043-9>
- Stephens, G. L., O'Brien, D., Webster, P. J., Pilewski, P., Kato, S., & Li, J. (2015). The albedo of Earth. *Reviews on Geophysics*, 53, 141–163. <https://doi.org/10.1002/2014RG000449>
- Su, W., Corbett, J., Eitzen, Z., & Liang, L. (2015a). Next-generation angular distribution models for top-of-atmosphere radiative flux calculation from CERES instruments: Methodology. *Atmospheric Measurement Techniques*, 8, 611–632. <https://doi.org/10.5194/amt-8-611-2015>

- Su, W., Corbett, J., Eitzen, Z., & Liang, L. (2015b). Next-generation angular distribution models for top-of-atmosphere radiative flux calculation from CERES instruments: Validation. *Atmospheric Measurement Techniques*, 8, 3297–3313. <https://doi.org/10.5194/amt-8-3297-2015>
- Sun, W., Loeb, N. G., Davies, R., Loukachine, K., & Miller, W. F. (2006). Comparison of MISR and CERES top-of-atmosphere albedo. *Geophysical Research Letters*, 33, L23810. <https://doi.org/10.1029/2006GL027958>
- Swartz, W., Lorentz, S., Papadakis, S., Huang, P., Smith, A., Deglau, D., et al. (2019). Ravan: CubeSat demonstration for multi-point Earth radiation budget measurements. *Remote Sensing*, 11(7), 796. <https://doi.org/10.3390/rs11070796>
- Trenberth, K. E. (2009). An imperative for climate change planning: Tracking Earth's global energy. *Current Opinion in Environmental Sustainability*, 1, 19–27. <https://doi.org/10.1016/j.cosust.2009.06.001>
- Wild, M., Folini, D., Hakuba, M. Z., Schar, C., Seneviratne, S. I., Kato, S., et al. (2015). The energy balance over land and oceans: An assessment based on direct observations and CMIP5 climate models. *Climate Dynamics*, 44, 3393–3429. <https://doi.org/10.1007/s00382-014-2430-z>
- World Geodetic System. (1984). Retrieved from <https://gisgeography.com/wgs84-world-geodetic-system/>
- Zhan, C., & Liang, S. (2022). Improved estimation of the global top-of-atmosphere albedo from AVHRR data. *Remote Sensing and Environment*, 269(112836). ISSN 0034-4257. <https://doi.org/10.1016/j.rse.2021.112836>
- Zhan, Y., Di Girolamo, L., Davies, R., & Moroney, C. (2018). Instantaneous top-of-atmosphere albedo comparison between CERES and MISR over the Arctic. *Remote Sensing*, 10, 1882. <https://doi.org/10.3390/rs10121882>